Title
Solution phase synthesis of indium gallium phosphide alloy nanowires.

Journal
ACS nano, 9(4)

ISSN
1936-0851

Authors
Kornienko, Nikolay
Whitmore, Desiré D
Yu, Yi
et al.

Publication Date
2015-04-01

DOI
10.1021/nn507335j

Peer reviewed

Solution Phase Synthesis of Indium Gallium Phosphide Alloy Nanowires

Nikolay Kornienko,[†] Desiré D. Whitmore,[†] Yi Yu,[†] Stephen R. Leone,[†,‡,∥] and Peidong Yang[*,†,§,⊥,#]

[†]Department of Chemistry, [‡]Department of Physics, and [§]Department of Materials Science Engineering, University of California, Berkeley, California 94720, United States, [∥]Chemical Sciences Division and [⊥]Materials Sciences Division, Lawrence Berkeley National Lab, Berkeley, California 94720, United States, and [#]Kavli Energy Nanosciences Institute, Berkeley, California 94720, United States

ABSTRACT The tunable physical and electronic structure of III−V semiconductor alloys renders them uniquely useful for a variety of applications, including biological imaging, transistors, and solar energy conversion. However, their fabrication typically requires complex gas phase instrumentation or growth from high-temperature melts, which consequently limits their prospects for widespread implementation. Furthermore, the need for lattice matched growth substrates in many cases confines the composition of the materials to a narrow range that can be epitaxially grown. In this work, we present a solution phase synthesis for indium gallium phosphide ($In_xGa_{1-x}P$) alloy nanowires, whose indium/gallium ratio, and consequently, physical and electronic structure, can be tuned across the entire $x = 0$ to $x = 1$ composition range. We demonstrate the evolution of structural and optical properties of the nanowires, notably the direct to indirect band gap transition, as the composition is varied from InP to GaP. Our scalable, low-temperature synthesis affords compositional, structural, and electronic tunability and can provide a route for realization of broader $In_xGa_{1-x}P$ applications.

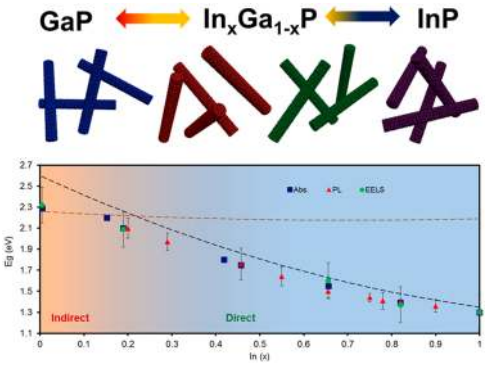

The III−V semiconductors are well sui-ted for a number of optoelectronic applications because of their typically high carrier mobilities and direct band gaps.[1] Among them, pseudobinary alloys of III−Vs feature structural and electronic properties such as band gap, index of refraction, and lattice constant that can be directly modified through the tuning of their composition.[2,3] Due to this unique control, III−V alloys find special uses in biomedical imaging,[4] light-emitting diodes,[5] lasers,[6] heterojunction bipolar transistors,[7] and high-performance multijunction photovoltaic cells.[8]

Indium gallium phosphide ($In_xGa_{1-x}P$) is a pseudobinary III−V alloy of an indirect band gap semiconductor, gallium phosphide (GaP), and a direct band gap semiconductor, indium phosphide (InP). This alloy possesses a tunable band gap that ranges from 1.35 to 2.26 electron volts (eV), which is direct for the composition range $1 \geq x \geq 0.2-0.3$.[9−11] The band gap range of 1.35−2.26 eV is particularly attractive for use in solar energy conversion and lighting applications because this range encompasses the majority of the visible light spectrum.[12] The ability to synthesize $In_xGa_{1-x}P$ in the nanowire (NW) morphology with tunable structural and electronic properties can pave a route toward potential applications in miniaturized optoelectronic devices, tunable NW lasers, and high surface area photocatalysts. However, there are several drawbacks that impede large-scale implementation of this material: bulk $In_xGa_{1-x}P$, thin films, or nanostructures are typically synthesized through liquid phase epitaxy (LPE), metal−organic chemical vapor deposition (MOCVD), or molecular beam epitaxy (MBE) techniques, which are coupled with several inherent limitations, including low material yield and expensive growth processes.[13] Furthermore, a common requirement for lattice matched substrates such as gallium arsenide (GaAs) or germanium (Ge) limits the composition range of the resulting materials to compositions that can grow epitaxially on these substrates.

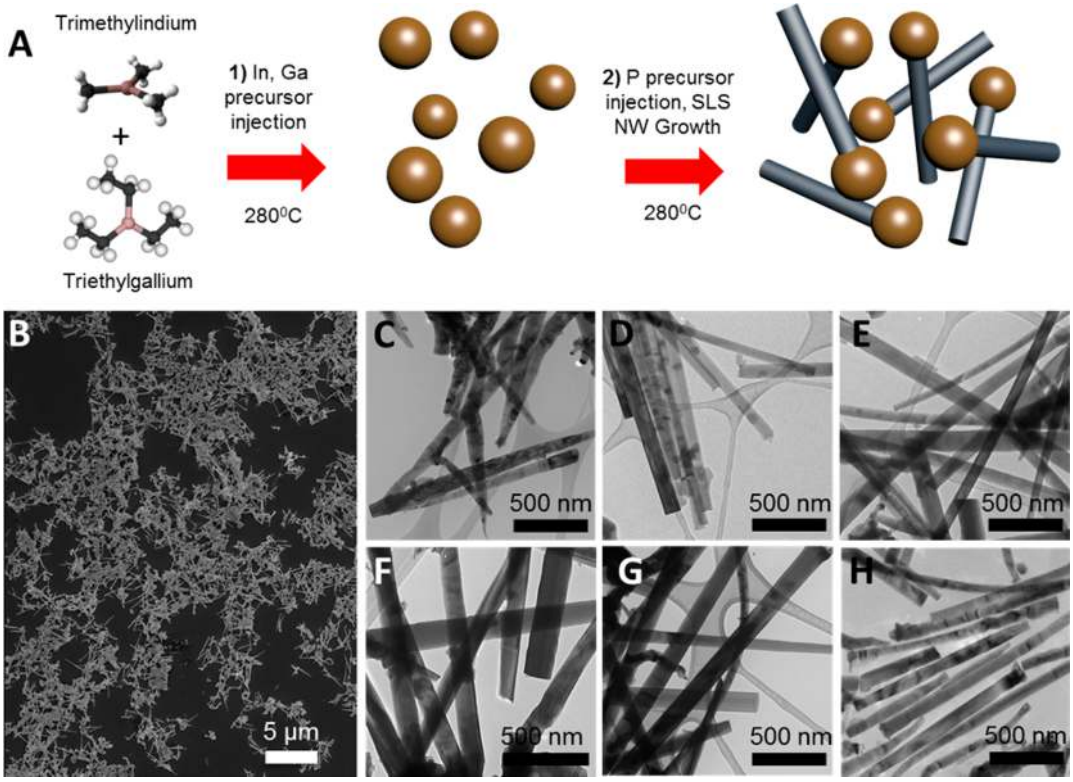

Figure 1. Synthetic scheme (A) of the $In_xGa_{1-x}P$ nanowire growth. SEM (B) of $In_xGa_{1-x}P$ NWs with $x = 0.50$ drop cast on a silicon substrate. TEM images of NWs (C−H) with composition $x = 0$, 0.21, 0.41, 0.66, 0.84, and 1.0, respectively.

In this work, we present a scalable, low-temperature solution phase synthesis for $In_xGa_{1-x}P$ NWs with full compositional, and therefore, structural and electronic tunability. In the recent literature, InP and GaP NWs were synthesized in the solution phase through a variety of techniques, including electrodeposition[14] and synthesis in aqueous solvents,[15] supercritical fluids,[16] and organic solvents.[17−24] Moreover, $Al_xGa_{1-x}As$ alloy NWs[25] and various II−VI NW alloys and heterostructures[26−28] have also been synthesized in the solution phase. $In_xGa_{1-x}P$ quantum dots have been synthesized through the thermal decomposition of precursors in an organic solvent.[29] $In_xGa_{1-x}P$ NWs, however, have been synthesized only through vapor phase CVD and MBE methods.[30−34] In light of the previous synthesis and applications of GaP, InP, and $In_xGa_{1-x}P$ NWs, we aimed at developing a solution phase synthesis of $In_xGa_{1-x}P$ NWs featuring (I) composition control, (II) low-temperature growth, (III) scalability, and (IV) no requirement for lattice matched substrates. In the following sections, we show that a preseeded solution−liquid−solid (SLS) synthesis can be used to controllably grow $In_xGa_{1-x}P$ NWs across the entire composition range of $x = 0$ to $x = 1$. Through systematic structural and optical measurements, we demonstrate structural and electronic tunability of $In_xGa_{1-x}P$ NWs and provide insight into both the disordered alloy crystal structure and the direct to indirect band gap transition.

RESULTS AND DISCUSSION

We synthesized $In_xGa_{1-x}P$ NWs with a one-pot, self-seeded SLS synthesis (Figure 1A) in a nitrogen environment using standard Schlenk line techniques. In this process, a liquid metal seed in solution serves as both the growth catalyst and group III precursor source. Trimethylindium (TMIn) and triethylgallium (TEGa) precursors were injected into a room-temperature, noncoordinating squalane solvent, and the solution was stirred until homogeneous. Next, the reaction mixture was lowered into a 280 °C molten salt bath and heated for 60 min to fully decompose the metal precursors and generate homogeneous indium−gallium alloy growth seeds. The In/Ga seed solution was next removed from the molten salt and allowed to cool to room temperature. After cooling, tris(trimethylsilyl)phosphine (TMSP) phosphorus precursor was then injected into the reactor, which was subsequently lowered into the same 280 °C molten salt bath and heated for an additional 60 min. The solution changed color from gray to black upon the growth of the $In_xGa_{1-x}P$ NWs. After thorough cleaning of the NWs through multiple centrifugation steps, a hydrochloric acid etch removed the metal seeds. Because TMIn and TEGa decompose at different rates under our reaction conditions, forming the In/Ga growth seeds in a separate step was necessary to obtain homogeneous $In_xGa_{1-x}P$ NWs. A mixture of

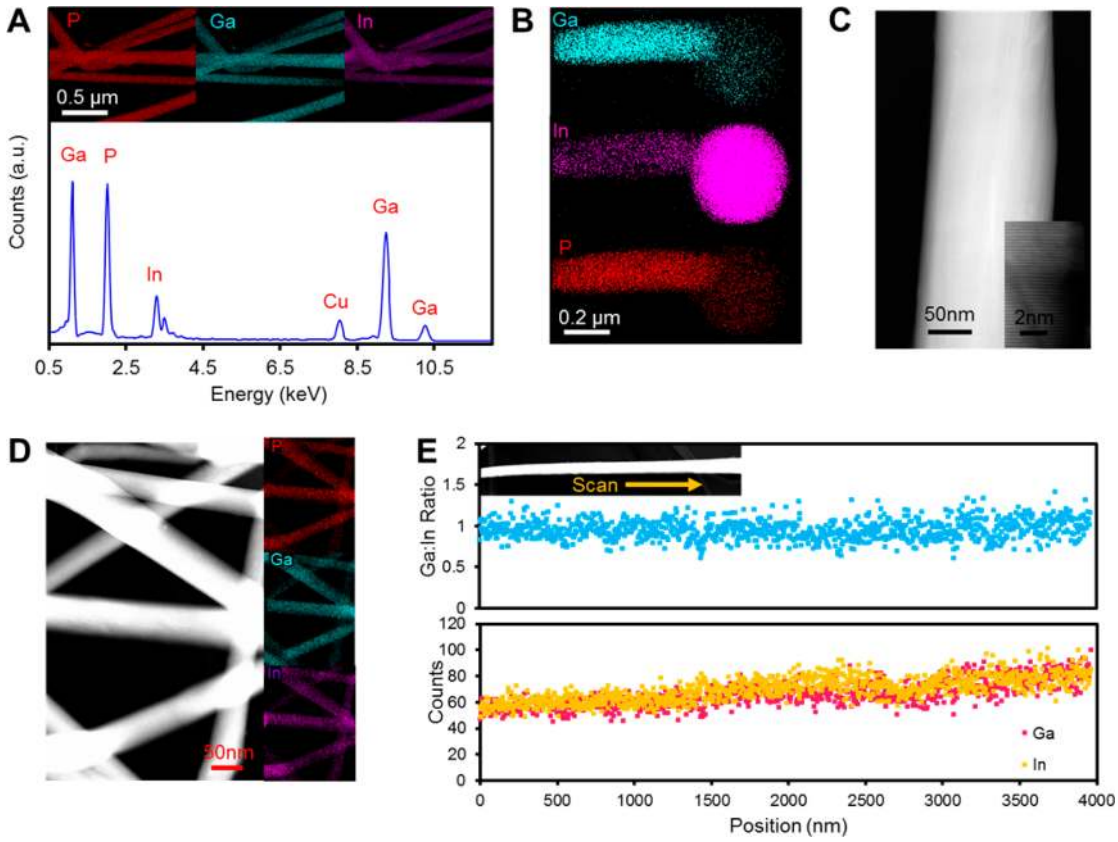

Figure 2. Electron microscopy analysis of $In_xGa_{1-x}P$ NWs. A typical EDS spectrum (A) featuring prominent In, Ga, and P peaks and their corresponding elemental maps in the inset. EDS map of a NW and growth seed (B) reveals an In-rich seed relative to the NW composition. Z-contrast HAADF-STEM of $In_xGa_{1-x}P$ NWs (C, D) with $x = 0.66$ and $x = 0.50$ features no abrupt contrast changes that would be indicative of sharp compositional fluctuations. A line scan along the length of the NW (E) shows no significant variations in the In/Ga elemental ratio though the possibility of compositional fluctuations of a few nanometers cannot be excluded.

separate InP and GaP NWs instead of alloys resulted when TMIn, TEGa, and TMSP precursors were mixed and heated in a single step (Figure S2).

Following the synthesis, we characterized the morphology and composition of the NWs with electron microscopy. The size and shape of the synthesized NWs were first studied with scanning electron microscopy (SEM). Figure 1B shows a typical SEM image of $In_xGa_{1-x}P$ NWs with a composition of $x = 0.50$. Transmission electron microscopy (TEM) in Figure 1C−H offers a closer look at the NWs and illustrates the morphology of several batches of NWs with different compositions. The diameters of the NWs typically varied between 70 and 150 nm, and their lengths between 1000 and 2500 nm. The composition of the NWs was controlled by the TMIn:TEGa ratio of the precursor, and the diameter of the NWs was controlled by the precursor concentration (Figure S3).

To assess the chemical composition and element distribution of the resulting NWs, scanning transmission electron microscopy energy dispersive X-ray spectroscopy (STEM-EDS) analysis was utilized. Figure 2A shows a typical EDS spectrum taken from $In_xGa_{1-x}P$ NWs, with $x = 0.21$, with Ga, In, and P peaks labeled, indicating the presence of both In and Ga in the NWs, with EDS mapping in the inset illustrating the corresponding elements distributed throughout the NWs. EDS mapping of an individual wire and growth seed (Figure 2B) reveals that the $In_xGa_{1-x}P$ NW was more Ga-rich than the growth seed, which was observed for every batch of alloy NWs. The tendency of $In_xGa_{1-x}P$ to grow as a more Ga-rich composition relative to the starting material is commonly observed and is explained by a lower formation enthalpy for the GaP relative to InP.[35−38] However, the NW body was uniform in composition: the lack of abrupt compositional variation is first evidenced in a lack of contrast in Z-contrast high-angle annular dark field scanning transmission electron microscopy (HAADF-STEM) in Figure 2C and D. Furthermore, a typical elemental line scan (Figure 2E) indicates that the composition of the NW generally remains uniform along the growth direction. However, with the techniques used, we cannot rule out fluctuations in composition of several nanometers or less.

We proceeded to study the structural properties, including crystal phase, growth direction, and presence or lack of long-range ordering of the $In_xGa_{1-x}P$

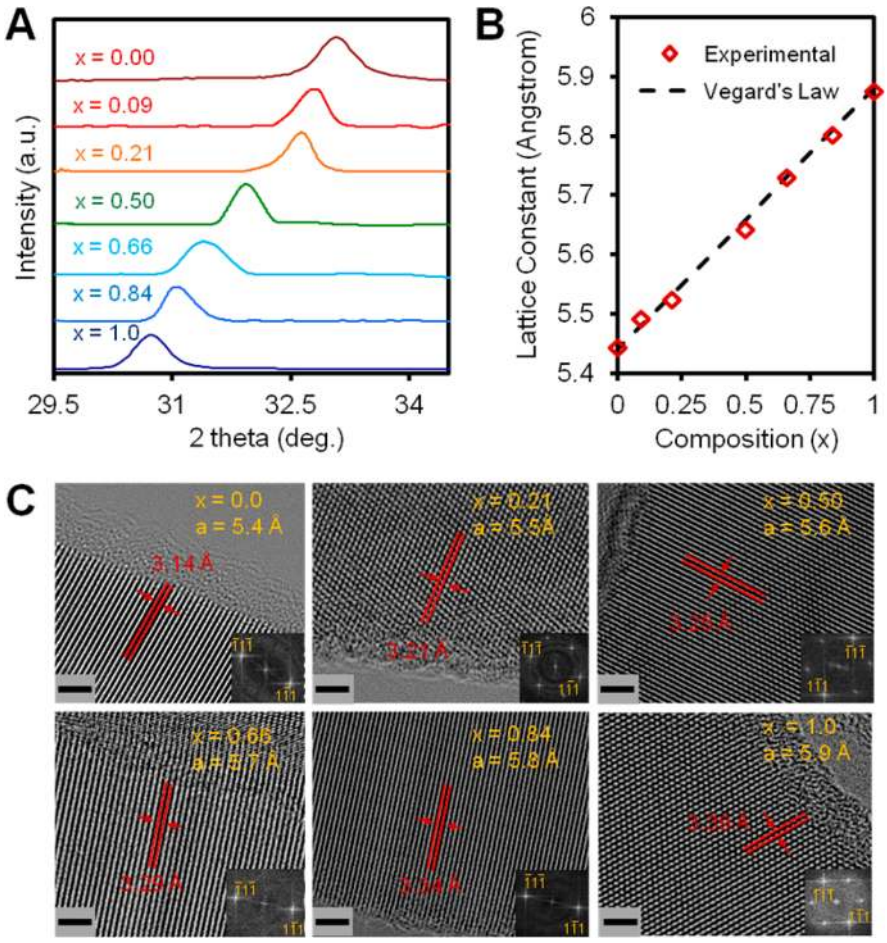

Figure 3. Powder XRD spectra (A) exhibit a shift in the (111) diffraction peak to larger 2 theta values with increasing Ga content, indicative of a lattice constant decrease. This lattice constant decrease is linear with composition, in accordance with Vegard's law (B). The lattice constant is additionally measured on single nanowires through analysis of HRTEM images (C), in which the FFT points corresponding to the (111) planes perpendicular to the growth direction were used for analysis.

through both microscopic and macroscopic methods. X-ray diffraction measurements (Figure S4) were first taken to determine the crystal structure of the NWs and indicate that the $In_xGa_{1-x}P$ NWs consist of a single phase zincblende structure across the entire composition range. There are several reports of wurtzite InP[39,40] and GaP[41] NWs grown in the vapor phase at high temperatures and large V/III precursor ratios. The formation of the wurtzite phase in these situations is believed to occur either in a regime of high growth temperature and precursor supersaturation in the catalyst where nucleation of the wurtzite phase is thermodynamically preferred, or for very thin NWs (with diameters typically less than 20 nm), where the relatively lower surface energy of wurtzite stabilizes this crystal phase.[42−44] However, our solution phase synthesis meets neither of these conditions, and only the zincblende phase is observed.

The lattice constant expansion of the $In_xGa_{1-x}P$ NWs from 5.45 Å to 5.88 Å with increasing indium composition, x, is measured at an ensemble level through shifting of the (111) peak to lower 2θ values, indicating larger distances between the corresponding crystal planes (Figure 3A). The full width at half maximum (fwhm) of the (111) diffraction peak, determined by instrument resolution, particle size, and crystal structure homogeneity, varies from 0.47 deg for InP and 0.58 deg for GaP up to a maximum 0.72 deg for $In_xGa_{1-x}P$ with x = 0.66. Considering that the size of our NWs is similar across the composition range and too large to significantly broaden the XRD peaks, our data are indicative of minor lattice constant fluctuations and a disordered crystal lattice in the $In_xGa_{1-x}P$ NWs. Asymmetries in the diffraction peaks may be due to the presence of dislocations, lattice strain, or fluctuations in composition within individual nanowires or within the batch.[33,45] The lattice constant of the NWs determined from the XRD measurements shifts linearly with NW composition in accordance with Vegard's law (Figure 3B), which predicts such a linear relation in an ensemble measurement of a random mixture where small structural fluctuations are averaged out.[46] The lack of significant deviations from Vegard's law or multiple (111) peaks in the XRD spectra indicates the absence of significant phase segregation in the $In_xGa_{1-x}P$ NWs.

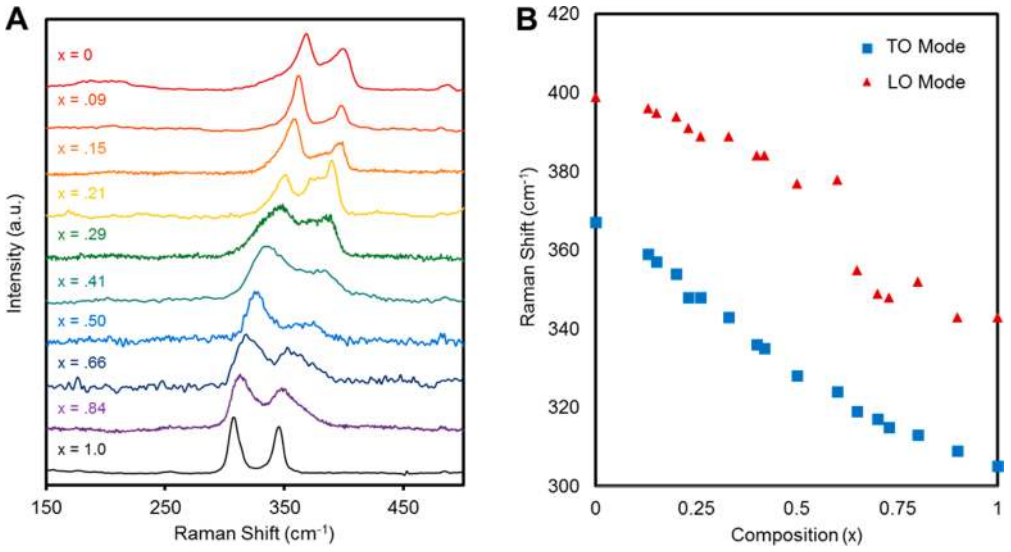

Figure 4. Evolution of the Raman spectrum of $In_xGa_{1-x}P$ NWs (A) shows a broadening of the phonon modes relative to InP and GaP, indicative of a disordered crystal structure. The $In_xGa_{1-x}P$ NW Raman spectra show a one-mode behavior (B), in which the frequency of the LO and TO phonon modes varies continuously with composition.

Macroscopic X-ray diffraction (XRD) structural measurements were accompanied by complementary TEM analysis on a microscopic level. Electron diffraction measurements of NWs viewed perpendicular to the [011] planes indicate that all NWs across the composition range grow along the ⟨111⟩ B thermodynamically preferred direction (Figure S5).[47,48] At high temperatures and slow growth rates, where precursor atoms can freely migrate on the surface during growth, $In_xGa_{1-x}P$ has a tendency to exhibit long-range ordering and superlattice formation. In this type of long-range ordering, typically called Cu−Pt ordering, (111) planes alternate between In-rich and Ga-rich composition, resulting in a superlattice, which is thought to be driven by surface reconstruction.[20,49−52] Initial evidence for a lack of long-range ordering in the $In_xGa_{1-x}P$ NWs in this work comes from the absence of superspots in the electron diffraction images, which have previously been used to demonstrate ordering in $In_xGa_{1-x}P$ thin films.[49,52] Alternating In-rich and Ga-rich planes would have also shown up as contrast lines perpendicular to the growth direction in the HAADF-STEM image of the NWs.[52]

The $In_xGa_{1-x}P$ lattice constant expansion with increasing indium composition is directly measured through high-resolution TEM (HRTEM) analysis (Figure 3C). Determined from the distance between (111) reciprocal lattice points in the Fourier transform of the HRTEM images, the lattice constant increases from ∼5.4 Å to ∼5.9 Å when the indium composition increases from $x = 0$ to $x = 1$. The complete structural tunability demonstrated from the self-seeded solution phase growth method developed in this work overcomes limitations commonly associated with MBE or LPE epitaxial growth, in which only a narrow $In_xGa_{1-x}P$ composition range can be synthesized.

Additional insight into compositional homogeneity and crystal structure was acquired with Raman spectroscopy, a technique that has been applied to $In_xGa_{1-x}P$ alloys to study the presence (or lack) of long-range order and elemental composition.[53−58] We first measured the Raman spectra of InP and GaP NWs and compared them to the corresponding bulk materials (Figure S6). The Raman spectrum of the NWs matches that of the bulk and exhibits two phonon modes: one transverse optical (TO) and one longitudinal optical (LO) mode. Next, we acquired Raman spectra and studied the corresponding modes for $In_xGa_{1-x}P$ across the composition range $0 \leq x \leq 1$ (Figure 4A) and noted three main phenomena: (I) The TO mode frequency linearly increases from 305 to 367 cm^{-1} with decreasing indium composition (Figure 4B), while the LO mode frequency has a relatively large shift at $x = 0.6$ but still varies continually from $x = 1$ to $x = 0$. This type of dispersion for the TO and LO modes has previously been reported in $In_xGa_{1-x}P$ as well as other alloys and was attributed to a one-mode behavior in which the phonon mode frequency continually shifts from the frequency of one pure material to another.[58,59] If the $In_xGa_{1-x}P$ alloys were composed of individual InP and GaP domains rather than a true alloy, then separate, distinct TO and LO modes would be expected, rather than a shift in frequency with composition. (II) The phonon modes for the $In_xGa_{1-x}P$ NWs are broadened compared to modes for InP and GaP, increasing in fwhm from 12 cm^{-1} up to 20 cm^{-1} for $x = 0.41$. This peak broadening has previously been attributed to a high degree of disorder in the material, suggesting the lack of long-range ordering and superlattice formation in the NWs.[57] (III) In studies of $In_xGa_{1-x}P$ with a high degree of long-range ordering and superlattice formation, an additional, sharp phonon mode at

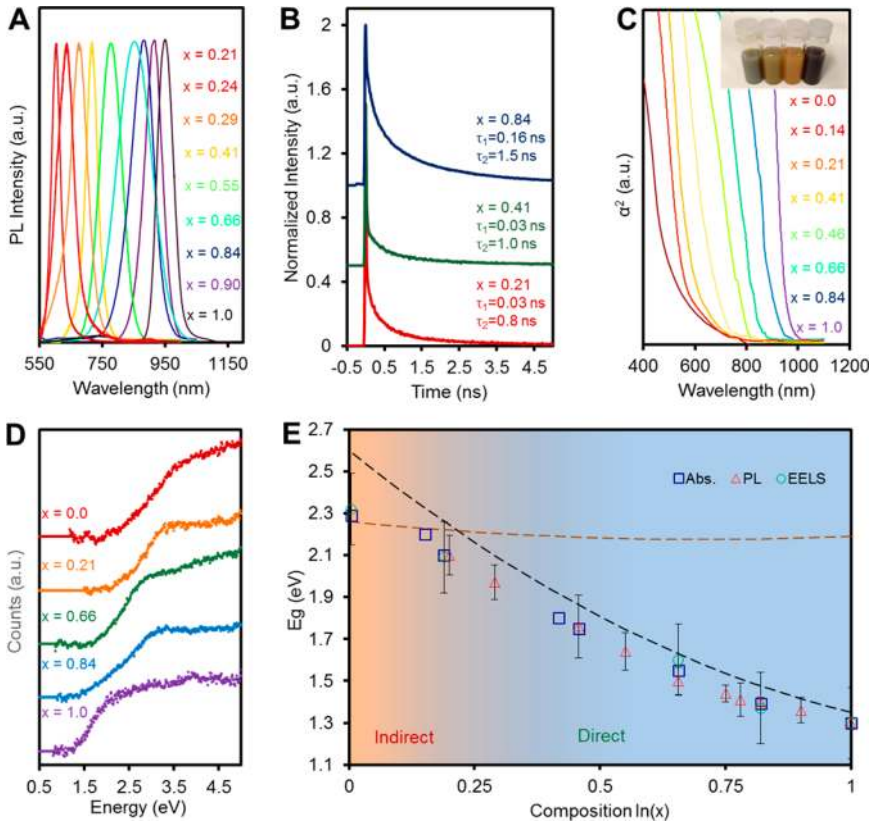

Figure 5. Band gap measurements of $In_xGa_{1-x}P$ NWs. PL spectra (A) illustrate an increase in band gap as the PL peak position blue-shifts with decreasing indium composition. Time-resolved PL spectra (B) show that NWs with $x > 0.2$ have lifetimes in line with those previously measured for direct band gap $In_xGa_{1-x}P$. UV−vis absorption spectra (C) also show a blue-shift with decreasing indium composition. The inset shows NWs with compositions $x = 0$, 0.14, 0.21, and $x = 0.41$ dispersed in acetone. EELS spectra (D) of NWs show an increase in onset energy with increasing gallium composition. Comprehensive band gap *vs* $In_xGa_{1-x}P$ composition (E) and the direct to indirect transition.

351−354 cm^{-1} appeared and was attributed to a longitudinal optical phonon due to the ⟨111⟩ long-range ordered superlattice in $In_xGa_{1-x}P$.[60−62] The lack of this feature in our spectra is consistent with our electron microscopy evidence for a disordered $In_xGa_{1-x}P$ crystal lattice.

Following the structural and Raman analysis, we focused on characterizing the optical and electronic properties of the $In_xGa_{1-x}P$ NWs. Of particular interest is the transition from an indirect to a direct band gap material, which is thought to occur at approximately $x = 0.25$ in the bulk.[32] To measure the evolution of the band gap with composition and to pinpoint this direct to indirect transition in our material, systematic band gap measurements were employed on both a macroscopic and microscopic level. First, the band gap was measured through the band-edge photoluminescence (PL) of the In_xGa_{1-x} NWs with various compositions (Figure 5A). The PL peak wavelength decreases from the near-infrared (NIR) to the visible range with decreasing indium composition, and strong PL emission at wavelengths as low as 580 nm can be detected for NWs with a composition $x = 0.21$. The diameter of the NWs is well above the ∼11 nm Bohr exciton radius of InP and GaP, so quantum confinement effects are not expected in our system and variations in PL emission wavelength are due to variations in NW composition.[19] Within the same batch of NWs, the PL peak energy varied slightly between individual wires, by approximately ±25 nm, indicative of small compositional variations within each batch.

Time-resolved photoluminescence (TRPL) spectra are plotted in Figure 5B for nanowires with compositions $x = 0.21$, 0.41, and 0.84. The PL decay kinetics are fit to a biexponential decay function with short component lifetimes of 0.034 ± 0.0006, 0.026 ± 0.0003, and 0.16 ± 0.004 ns and long component lifetimes of 0.78 ± 0.008, 0.96 ± 0.01, and 1.51 ± 0.02 ns for NWs with compositions $x = 0.21$, 0.41, and 0.84, respectively. A biexponential fit with a slow component of 0.5−2.0 ns is typical for radiative band to band recombination in a direct band gap semiconductor, and the measured lifetimes are consistent with those previously reported for direct band gap $In_xGa_{1-x}P$ of 1−3 ns.[63,64] This provides additional evidence that the luminescence observed is from a band to band radiative recombination as opposed to processes such as defect emission or indirect band gap emission, which have radiative lifetimes on the order of tens of nanoseconds to microseconds.[41,65] The control

of PL emission from the visible to NIR energy range is expected to have applications toward tunable $In_xGa_{1-x}P$-based LEDs and NW lasers.

The band gap of the NWs was next recorded with UV−vis−NIR absorption measurements using an integrating sphere setup. Figure 5C shows the absorption spectra of thin NW films deposited onto transparent glass substrates, where the absorption edge blue-shifts with decreasing indium composition, x, and increasing band gap, from the NIR to the visible energy range. Samples with a composition of $x \geq 0.21$ featured a sharp increase in absorption at the band edge, consistent with the typical absorption profile of a direct band gap material. In contrast, the samples with $x < 0.21$ have indirect band gaps and feature slowly increasing absorption and only a sharp absorption increase at higher energies where their direct band gap lies (Figure S7).

Microscopic band gap measurements were next employed through monochromatic, low-loss, electron energy loss spectroscopy (EELS). A unique advantage of EELS is the ability to obtain the electronic structure of materials with a very high spatial resolution, rendering this technique uniquely suitable for single NW studies.[66] In these measurements, inelastically scattered electrons are measured and the band gap is typically determined by the position of the energy onset of the electron loss peak in the low-loss region (0−10 eV). Because such a measurement will be affected by parameters like material thickness and instrument configuration, all parameters were kept consistent across the measurements. After measurement, the band gap was extracted from the raw data through a commonly used power law fit peak subtraction method.[67] Processed EELS data from wires with varying composition are plotted in Figure 5D, with GaP and InP NWs serving as internal standards to verify our measurement and method of band gap determination. Our low-loss EELS data show that the band-edge electron energy loss peak onset shifts from 1.35 eV for InP wires to 2.30 eV for GaP wires, with $In_xGa_{1-x}P$ alloys having band gaps intermediate between the two, which is consistent with our PL and absorption data. Because different EELS processing methods can yield varying results, an alternate method to extract the band gap was used and gave similar results (Figure S8).

In addition to band gap quantification, low-loss EELS measurements can reveal the nature of interband transitions (direct *vs* indirect) and are used in this work as a complementary technique to determine the direct to indirect band crossover. The slope of the EELS onset peak for interband transitions is determined by the valence and conduction band joint density of states (JDOS).[67] For direct band gap semiconductors, the JDOS, and consequently the EELS signal intensity at energies greater than the band gap (E_g), increases as $(E - E_g)^{1/2}$. The EELS onset for InP NWs is fit using this direct band gap function (Figure S9). For indirect band gap materials, the EELS signal is proportional to the JDOS of indirect band gap semiconductors, which follows a $(E - E_g)^{3/2}$ relation, and the EELS data for GaP NWs are fit using the $(E - E_g)^{3/2}$ function. $In_xGa_{1-x}P$ alloy EELS data were next analyzed, and the direct to indirect transition is observed through the EELS onset changing from an $E^{3/2}$ to an $E^{1/2}$ shape at compositions of $x = 0.21$. At this composition, there are contributions to the signal from both direct and indirect transitions, resulting in a seemingly linear intensity increase and an imperfect fit using either model. However, when x is continually increased, the slope of the EELS peak resembles more the $E^{1/2}$ relation, as the direct band gap becomes the primary transition.

The comprehensive band gap measurements from PL, absorption, and EELS measurements are plotted as a function of composition in Figure 5E along with the calculated band gap using literature values. PL measurements correlating with individual NW composition were also acquired and follow a similar trend (Figure S10). For $In_xGa_{1-x}P$, the band gap changes from direct to indirect at $x \approx 0.21$, when the lowest energy point in the conduction band changes from the Γ valley (direct) to the X valley (indirect).[32] The transition from direct to indirect band gap can also be pinpointed through the analysis of the volume-normalized PL intensity as a function of PL energy (Figure S11).[9,68,69] The band gap energy value is not linear with composition but bowed due to microscopic fluctuations in local strain, core potentials, and other nearest neighbor effects that lead to a deviation from a perfectly periodic potential felt by electrons.[70] As a result, the band gap, $E_\Gamma(X)$, as a function of composition, X, of an alloy of materials A and B follows the relation $E_\Gamma(X) = E_\Gamma^A(X) + E_\Gamma^B(1 - X) - cX(1 - X)$ where c is the bowing parameter and $E_\Gamma{}^A$ and $E_\Gamma{}^B$ are the band gaps for materials A and B. For $In_xGa_{1-x}P$, the bowing parameters of 0.65 and 0.2, taken from previous literature reports, were used to calculate the Γ (direct) and X (indirect) band gaps, respectively.[71] Our experimental data from PL, absorption, and EELS follow these calculated values. The correspondence between predicted and experimental band gap energies is a promising demonstration of controllable electronic tunability that is offered through this solution phase $In_xGa_{1-x}P$ NW synthesis.

CONCLUSION

In conclusion, we have developed a novel synthetic approach to obtain fully tunable $In_xGa_{1-x}P$ NWs *via* a preseeded solution phase synthesis. Using complementary macroscopic and microscopic measurements, we have demonstrated access to every composition across the $0 \leq x \leq 1$ range. XRD and TEM measurements demonstrate a tunable lattice constant, while electron diffraction and Raman spectroscopic

measurements indicate that the $In_xGa_{1-x}P$ NWs are likely a disordered alloy and do not feature significant long-range ordering or superlattice formation. The band gap tunability and change from direct to indirect band gap were measured through PL, optical absorption, and EELS measurements. While this work focuses on $In_xGa_{1-x}P$, our synthetic method can potentially be applied to other alloy systems with precursors compatible with the synthetic conditions, opening up a new avenue to access and utilize III−V, II−VI, and other alloys *via* a low-temperature scalable synthesis.

METHODS

Chemicals. Trimethylindium (TMIn, 98%, Strem), triethylgallium (TEGa, 98%, Strem), tris(trimethylsilyl)phosphine (TMSP, min. 98%, Strem), and squalane (98%, Alfa Aesar) were purchased and used as received.

Preparation of Stock 0.2 mmol/g TMIn, TEGa, and TMSP Solutions. Squalane was first degassed and dried at 60 °C under vacuum for 90 min in an air-free glass reactor. Individual 0.2 mmol/g precursor solutions of TMSP and TEGa were prepared in a nitrogen environment glovebox by diluting the respective chemicals in squalane and stirring for at least 4 h at room temperature to ensure they were fully dissolved. A 0.2 mmol/g precursor solution of TMIn was prepared by mixing TMIn powder with 1-octadecene. This mixture was stirred for at least 4 h at room temperature.

Synthesis of $In_xGa_{1-x}P$ Nanowires in Squalane. Nanowires were synthesized in a nitrogen environment in 50 mL air-free glass reactors using standard Schlenk line techniques. In a typical preparation, 5 g of squalane solvent was loaded into the reactor and degassed under vacuum for 30 min; then the reactor was filled with nitrogen. The TMIn and TEGa stock solutions (0.5 g total) were injected into the reactor and stirred for ~3 min. The flask was next inserted into a preheated salt bath ($NaNO_3$/KNO_3, 46/54 by weight) at 280 °C. After ~90 s, the color of the reaction mixture changed to milky gray, indicating formation of In/Ga nanoparticles. After at least 1 h of heating and stirring at 60 rpm to homogenize the particles, the solution was cooled and 0.5 g of TMSP stock solution was injected. The reactor was then submerged again into the 280 °C salt bath, then withdrawn after 60 min of reacting and allowed to cool to room temperature.

Isolation and Purification of $In_xGa_{1-x}P$ Nanowires. The $In_xGa_{1-x}P$ nanowires were isolated by centrifugation at 12 000 rpm. The isolated $In_xGa_{1-x}P$ wires were next redispersed in hexanes, sonicated, and isolated again through centrifugation. This procedure was performed several times to thoroughly clean the nanowires. The cleaned wires were next dispersed in ethanol and vacuum filtered through a 0.22 μm PVDF membrane and dried under ambient conditions.

Etching of In/Ga Nanoparticles. The dried $In_xGa_{1-x}P$ nanowires were dispersed in 0.02 M hydrochloric acid and sonicated for several hours to completely etch away the metal tips. After sonicating for several hours, the NWs were again isolated through centrifugation and dispersed in DI water. This was performed several times. The aqueous nanowire dispersion of $In_xGa_{1-x}P$ nanowires was filtered again through a 0.22 μm PVDF membrane and dried under ambient conditions.

Raman Spectroscopy. Raman measurements were taken with a laser confocal Raman system (Horiba JY LabRAM HR; diode pumped-Nd:YAG laser, 532 nm, 0.2 W, unpolarized), with an Olympus SLMPLN 50 long-distance objective. To minimize local heating and sample damage, a D2 neutral density filter was utilized to reduce the laser intensity on the sample by a factor of 100. A grating of 1800 grooves/mm was utilized, resulting in a spectral resolution of 1 cm^{-1}. Ten seconds was used as a typical acquisition time. Photoluminescence measurements were taken on the same setup, except that a 600 grooves/mm grating was used. All measurements were conducted at room temperature

Time-Resolved Photoluminescence Measurement. Photoluminescence decay times were measured, using a home-built confocal microscope (Olympus IX71 base), for nanowires of varying indium to gallium concentration ratios. Nanowire samples were drop-cast onto one-inch-diameter UV-fused silica microscope coverslips. A frequency-doubled titanium-sapphire regenerative amplifier (Coherent RegA 9000) output at 400 nm was used as the excitation source, with ~150 fs pulses at a 300 kHz repetition rate. Approximately 1% of the excitation source was picked off and sent into a fast photodiode for accurate timing of the laser pulse arrival time. The remainder of the source was attenuated using a series of neutral density filters to obtain powers ranging from 10 nW to 200 mW (this seems to be a huge range of powers?) and focused on the nanowire cluster with an oil-immersion objective lens (Nikon PlanFluor, NA = 1.3) to a spot size of ~700 μm. The PL emission was collected in an epi-configuration using the same lens and directed through a 420 nm long-wave-pass dichroic mirror before being focused onto a single-photon avalanche photodiode detector (APD, PDM series, Micro Photon Devices). The band-edge emission from the nanowires was further isolated using band-pass filters prior to detection. The fast photodiode and APD signals were read into a time-correlated single photon counting card (PicoHarp300, PicoQuant). The timing card collected photon arrival times in 32 ps bins, and the instrument response function was measured to have a fwhm of ~42 ps.

Low-Loss Monochromatic Electron Energy Loss Spectroscopy. STEM-EELS was performed using a FEI Tecnai F20 UT electron microscope operated at 200 kV in the National Center of Electron Microscopy (NCEM), Lawrence Berkeley National Laboratory. The probe size was 1 nm. The fwhm of the zero-loss peak (ZLP) was optimized at 0.17 eV. The fwhm of the ZLP effectively determines the energy resolution for the band gap measurements. The energy dispersion was set to 0.01 eV to obtain a 20 eV spectrum width, and the acquisition time for EELS spectra was set to 0.2 s. Convergence and collection angles of 21 and 42 mrad were used, respectively. The camera length was set to 52 mm, and a GIF entrance aperture of 2.5 mm was used. To remove the zero-loss peak and extract the inelastically scattered electrons in Figure 5, a power-law fit peak subtraction procedure was performed in Digital Micrograph (Gatan Inc.). Because of the exact method of data processing and band gap extraction, the procedure may affect the end result. Thus, the band gap was measured through an additional method. In addition to the power-law fit, band gaps were determined from the inflection point in the raw data. At these low-loss levels, Cherenkov radiation gave rise to a high-energy shoulder on the ZLP and led to a slightly higher measured band gap when using this method, but the overall trend was consistent.

Conflict of Interest: The authors declare no competing financial interest.

Supporting Information Available: Experimental details, electron microscopy data, and spectroscopic data. This material is available free of charge *via* the Internet at http://pubs.acs.org.

Acknowledgment. This work was supported by the Office of Science, Office of Basic Energy Sciences of the U.S. Department of Energy under Contract No. DE-AC02-05CH11231 (PChem). Electron microscopy was performed at NCEM, which is supported by the Office of Science, Office of Basic Energy Sciences of the U.S. Department of Energy under Contract No. DE-AC02-05CH11231.

REFERENCES AND NOTES

1. Adachi, S. Front Matter. In *Physical Properties of III-V Semiconductor Compounds*; Wiley & Co: New York, 2005; pp i−xviii.

2. Adachi, S. Front Matter. In *Properties of Semiconductor Alloys*; John Wiley & Sons, Ltd: New York, 2009; pp i−xxii.
3. Linnik, M.; Christou, A. Calculations of Optical Properties for Quaternary III-V Semiconductor Alloys in the Transparent Region and above 0.2 eV. *Phys. B* **2002**, *318*, 140–161.
4. Vandersmissen, R.; Merken, P. High-Resolution InGaAs Sensor Pushing Biomedical Infrared Optical Coherence Tomography. *Adv. Opt. Technol.* **2013**, *2*, 241.
5. Timmons, M. L.; Katsuyama, T.; Sillmon, R.; Bedair, S. M. In *GaAsP-InGaAs Superlattice Light-Emitting Diodes*; Electron Devices Meeting, 1983 International, 1983; pp 692−695.
6. Mascarenhas, A.; Zhang, Y. Dilute Nitride Based III,V Alloys for Laser and Solar Cell Applications. *Curr. Opin. Solid State Mater. Sci.* **2001**, *5*, 253–259.
7. Palankovski, V.; Schultheis, R.; Selberherr, S. Simulation of Power Heterojunction Bipolar Transistors on Gallium Arsenide. *IEEE Trans. Electron Devices* **2001**, *48*, 1264–1269.
8. Strobl, G. F.; Bergunde, T.; Kostler, W.; Kern, R.; Meusel, M.; LaRoche, G.; Zimmermann, W.; Bett, A. W.; Dimroth, F.; Geens, W.; *et al*. *European Roadmap of Multijunction Solar Cells and Qualification Status*; Photovoltaic Energy Conversion, Conference Record of the 2006 IEEE 4th World Conference, May **2006**; pp 1793−1796.
9. Onton, A.; Lorenz, M.; Reuter, W. Electronic Structure and Luminescence Processes in In1−xGaxP Alloys. *J. Appl. Phys.* **1971**, *42*, 3420–3432.
10. Onton, A.; Chicotka, R. Photoluminescence Processes in In1-xGaxP at 2° K. *Phys. Rev. B: Solid State* **1971**, *4*, 1847.
11. Lorenz, M.; Reuter, W.; Dumke, W.; Chicotka, R.; Pettit, G.; Woodall, J. Band Structure and Direct Transition Electroluminescence in the In1-xGaxP Alloys. *Appl. Phys. Lett.* **1968**, *13*, 421–423.
12. Khaselev, O.; Turner, J. A. A Monolithic Photovoltaic-Photoelectrochemical Device for Hydrogen Production *via* Water Splitting. *Science* **1998**, *280*, 425–427.
13. Prutskij, T.; Arencibia, P.; Brito-Orta, R. A.; Mintairov, A.; Kosel, T.; Merz, J. Luminescence Anisotropy of InGaP Layers Grown by Liquid Phase Epitaxy. *J. Phys. D: Appl. Phys.* **2004**, *37*, 1563.
14. Dorn, A.; Allen, P. M.; Bawendi, M. G. Electrically Controlling and Monitoring InP Nanowire Growth from Solution. *ACS Nano* **2009**, *3*, 3260–3265.
15. Xiong, Y.; Xie, Y.; Li, Z.; Li, X.; Gao, S. Aqueous-Solution Growth of GaP and InP Nanowires: A General Route to Phosphide, Oxide, Sulfide, and Tungstate Nanowires. *Chem.−Eur. J.* **2004**, *10*, 654–660.
16. Davidson, F. M.; Wiacek, R.; Korgel, B. A. Supercritical Fluid-Liquid-Solid Synthesis of Gallium Phosphide Nanowires. *Chem. Mater.* **2005**, *17*, 230–233.
17. Lim, T. H.; Ravi, S.; Bumby, C. W.; Etchegoin, P. G.; Tilley, R. D. Synthesis, Characterization and Photoconductivity of Highly Crystalline InP Nanowires Prepared from Solid Hydrogen Phosphide. *J. Mater. Chem.* **2009**, *19*, 4852–4856.
18. Trentler, T. J.; Hickman, K. M.; Goel, S. C.; Viano, A. M.; Gibbons, P. C.; Buhro, W. E. Solution-Liquid-Solid Growth of Crystalline III-V Semiconductors: An Analogy to Vapor-Liquid-Solid Growth. *Science* **1995**, *270*, 1791–1794.
19. Yu, H.; Li, J.; Loomis, R. A.; Wang, L.-W.; Buhro, W. E. Two *versus* Three-Dimensional Quantum Confinement in Indium Phosphide Wires and Dots. *Nat. Mater.* **2003**, *2*, 517–520.
20. Sun, J.; Liu, C.; Yang, P. Surfactant-Free, Large-Scale, Solution,Liquid,Solid Growth of Gallium Phosphide Nanowires and Their Use for Visible-Light-Driven Hydrogen Production from Water Reduction. *J. Am. Chem. Soc.* **2011**, *133*, 19306–19309.
21. Liu, Z.; Sun, K.; Jian, W. B.; Xu, D.; Lin, Y. F.; Fang, J. Soluble InP and GaP Nanowires: Self-Seeded, Solution−Liquid−Solid Synthesis and Electrical Properties. *Chem.−Eur. J.* **2009**, *15*, 4546–4552.
22. Trentler, T. J.; Goel, S. C.; Hickman, K. M.; Viano, A. M.; Chiang, M. Y.; Beatty, A. M.; Gibbons, P. C.; Buhro, W. E. Solution-Liquid-Solid Growth of Indium Phosphide Fibers from Organometallic Precursors: Elucidation of Molecular
23. Strupeit, T.; Klinke, C.; Kornowski, A.; Weller, H. Synthesis of InP Nanoneedles and Their Use as Schottky Devices. *ACS Nano* **2009**, *3*, 668–672.
24. Banerjee, C.; Hughes, D. L.; Bochmann, M.; Nann, T. InP Nanowires from Surfactant-Free Thermolysis of Single Molecule Precursors. *Dalton Trans.* **2012**, *41*, 7244–7248.
25. Markowitz, P. D.; Zach, M. P.; Gibbons, P. C.; Penner, R.; Buhro, W. E. Phase Separation in AlxGa1-xAs Nanowhiskers Grown by the Solution-Liquid-Solid Mechanism. *J. Am. Chem. Soc.* **2001**, *123*, 4502–4511.
26. Laocharoensuk, R.; Palaniappan, K.; Smith, N. A.; Dickerson, R. M.; Werder, D. J.; Baldwin, J. K.; Hollingsworth, J. A. Flow-Based Solution-Liquid-Solid Nanowire Synthesis. *Nat. Nanotechnol.* **2013**, *8*, 660–666.
27. Zhu, G.; Xu, Z. Controllable Growth of Semiconductor Heterostructures Mediated by Bifunctional Ag_2S Nanocrystals as Catalyst or Source-Host. *J. Am. Chem. Soc.* **2010**, *133*, 148–157.
28. Ouyang, L.; Maher, K. N.; Yu, C. L.; McCarty, J.; Park, H. Catalyst-Assisted Solution-Liquid-Solid Synthesis of CdS/CdSe Nanorod Heterostructures. *J. Am. Chem. Soc.* **2007**, *129*, 133–138.
29. Mićić, O.; Nozik, A. Synthesis and Characterization of Binary and Ternary III−V Quantum Dots. *J. Lumin.* **1996**, *70*, 95–107.
30. Fakhr, A.; Haddara, Y.; LaPierre, R. Dependence of InGaP Nanowire Morphology and Structure on Molecular Beam Epitaxy Growth Conditions. *Nanotechnology* **2010**, *21*, 165601.
31. Svensson, C. P. T.; Mårtensson, T.; Trägårdh, J.; Larsson, C.; Rask, M.; Hessman, D.; Samuelson, L.; Ohlsson, J. Monolithic GaAs/InGaP Nanowire Light Emitting Diodes on Silicon. *Nanotechnology* **2008**, *19*, 305201.
32. Wallentin, J.; Poncela, L. B.; Jansson, A. M.; Mergenthaler, K.; Ek, M.; Jacobsson, D.; Wallenberg, L. R.; Deppert, K.; Samuelson, L.; Hessman, D. Single GaInP Nanowire PIN Junctions near the Direct to Indirect Bandgap Crossover Point. *Appl. Phys. Lett.* **2012**, *100*, 251103.
33. Kriegner, D.; Persson, J. M.; Etzelstorfer, T.; Jacobsson, D.; Wallentin, J.; Wagner, J. B.; Deppert, K.; Borgström, M.; Stangl, J. Structural Investigation of GaInP Nanowires Using X-Ray Diffraction. *Thin Solid Films* **2013**, *543*, 100–105.
34. Ishizaka, F.; Ikejiri, K.; Tomioka, K.; Fukui, T. Indium-Rich InGaP Nanowires Formed on InP (111) a Substrates by Selective-Area Metal Organic Vapor Phase Epitaxy. *Jpn. J. Appl. Phys.* **2013**, *52*, 04CH05–04CH05−4.
35. Willardson, R. K.; Beer, A. C. *Semiconductor Semimetals*; Academic Press: New York, 1977; Vol. 12.
36. Weast, R. C.; Astle, M. J.; Beyer, W. H. *CRC Handbook of Chemistry and Physics*; CRC Press: Boca Raton, FL, 1988; Vol. 69.
37. Vasil'ev, V.; Gachon, J.-C. Thermodynamic Properties of InP. *Inorg. Mater.* **2006**, *42*, 1171–1175.
38. Sirota, N.; Makovatskaya, I.; Rozov, V.; Vitkana, T. Z. *Chemical Bonds in Solids*; Springer: Berlin, 1972; Vol. 2.
39. Kriegner, D.; Wintersberger, E.; Kawaguchi, K.; Wallentin, J.; Borgström, M.; Stangl, J. Unit Cell Parameters of Wurtzite InP Nanowires Determined by X-Ray Diffraction. *Nanotechnology* **2011**, *22*, 425704.
40. Joyce, H. J.; Wong-Leung, J.; Gao, Q.; Tan, H. H.; Jagadish, C. Phase Perfection in Zinc Blende and Wurtzite III−V Nanowires Using Basic Growth Parameters. *Nano Lett.* **2010**, *10*, 908–915.
41. Assali, S.; Zardo, I.; Plissard, S.; Kriegner, D.; Verheijen, M.; Bauer, G.; Meijerink, A.; Belabbes, A.; Bechstedt, F.; Haverkort, J. Direct Band Gap Wurtzite Gallium Phosphide Nanowires. *Nano Lett.* **2013**, *13*, 1559–1563.
42. Glas, F.; Harmand, J.-C.; Patriarche, G. Why Does Wurtzite Form in Nanowires of III-V Zinc Blende Semiconductors? *Phys. Rev. Lett.* **2007**, *99*, 146101.
43. Johansson, J.; Karlsson, L. S.; Dick, K. A.; Bolinsson, J.; Wacaser, B. A.; Deppert, K.; Samuelson, L. Effects of

Supersaturation on the Crystal Structure of Gold Seeded III−V Nanowires. *Cryst. Growth Des.* **2008**, *9*, 766–773.
44. Johansson, J.; Dick, K.; Caroff, P.; Messing, M.; Bolinsson, J.; Deppert, K.; Samuelson, L. Diameter Dependence of the Wurtzite−Zinc Blende Transition in InAs Nanowires. *J. Phys. Chem. C* **2010**, *114*, 3837–3842.
45. Akimoto, K.; Emoto, T. Quantitative Strain Analysis of Surfaces and Interfaces Using Extremely Asymmetric X-Ray Diffraction. *J. Phys.: Condens. Matter* **2010**, *22*, 473001.
46. Denton, A. R.; Ashcroft, N. W. Vegard's Law. *Phys. Rev. A: At., Mol., Opt. Phys.* **1991**, *43*, 3161.
47. Fortuna, S. A.; Li, X. Metal-Catalyzed Semiconductor Nanowires: A Review on the Control of Growth Directions. *Semicond. Sci. Technol.* **2010**, *25*, 024005.
48. Mattila, M.; Hakkarainen, T.; Jiang, H.; Kauppinen, E.; Lipsanen, H. Effect of Substrate Orientation on the Catalyst-Free Growth of InP Nanowires. *Nanotechnology* **2007**, *18*, 155301.
49. Fetzer, C.; Lee, R.; Shurtleff, J.; Stringfellow, G.; Lee, S.; Seong, T. The Use of a Surfactant (Sb) to Induce Triple Period Ordering in GaInP. *Appl. Phys. Lett.* **2000**, *76*, 1440–1442.
50. Song, J.; Ok, Y.-W.; Kim, J.; Lee, Y.; Seong, T.-Y. Occurrence of CuPt-a and CuPt-B Type Ordering in GaInP Layers Grown by Solid Source Molecular Beam Epitaxy. *Appl. Surf. Sci.* **2001**, *183*, 33–38.
51. Philips, B.; Norman, A.; Seong, T.; Mahajan, S.; Booker, G.; Skowronski, M.; Harbison, J.; Keramidas, V. Mechanism for CuPt-Type Ordering in Mixed III−V Epitaxial Layers. *J. Cryst. Growth* **1994**, *140*, 249–263.
52. Ahrenkiel, S.; Jones, K.; Matson, R.; Al-Jassim, M.; Zhang, Y.; Mascarenhas, A.; Friedman, D.; Arent, D.; Olson, J.; Hanna, M. CuPt-B Ordered Microstructures in GaInP and GaInAs Films, *Mater. Res. Soc. Symp. Proc.*; Cambridge Univ Press, 1999; p 243.
53. González, L.; González, Y.; Dotor, M. L.; Martinez-Pastor, J. Optical Characterization of Disordered InxGa1−xP Alloys. *Appl. Phys. Lett.* **1998**, *72*, 2595–2597.
54. Nakaema, M. K. K.; Godoy, M. P. F.; Brasil, M. J. S. P.; Iikawa, F.; Silva, D.; Sacilotti, M.; Decobert, J.; Patriarche, G. Optical and Structural Investigation of InxGaxP Free-Standing Microrods. *J. Appl. Phys.* **2005**, *98*, 053506.
55. Kato, T.; Matsumoto, T.; Ishida, T. Raman Spectral Behavior of In1-xGaxP ($0 < x < 1$). *Jpn. J. Appl. Phys.* **1988**, *27*, 983.
56. Zachau, M.; Masselink, W. Luminescence and Raman Measurements of InyGa1−yP ($0.3 < y < 0.5$) Grown by Gas-Source Molecular Beam Epitaxy. *Appl. Phys. Lett.* **1992**, *60*, 2098–2100.
57. Abdelouhab, R.; Braunstein, R.; Bärner, K.; Rao, M.; Kroemer, H. Raman Scattering in a Ga1−xInxP Strained Heterostructure. *J. Appl. Phys.* **1989**, *66*, 787–792.
58. Lucovsky, G.; Brodsky, M. H.; Chen, M. F.; Chicotka, R. J.; Ward, A. T. Long-Wavelength Optical Phonons in InxGa1-xP. *Phys. Rev. B: Solid State* **1971**, *4*, 1945–1949.
59. Chang, I.; Mitra, S. Application of a Modified Random-Element-Isodisplacement Model to Long-Wavelength Optic Phonons of Mixed Crystals. *Phys. Rev.* **1968**, *172*, 924.
60. Cheong, H. M.; Mascarenhas, A.; Ernst, P.; Geng, C. Effects of Spontaneous Ordering on Raman Spectra of GaInP 2. *Phys. Rev. B: Condens. Matter Mater. Phys.* **1997**, *56*, 1882.
61. Alsina, F.; Mestres, N.; Pascual, J.; Geng, C.; Ernst, P.; Scholz, F. Raman Scattering in Single-Variant Spontaneously Ordered GaInP2. *Phys. Rev. B: Condens. Matter Mater. Phys.* **1996**, *53*, 12994.
62. Mintairov, A.; Merz, J.; Vlasov, A.; Vinokurov, D. Observation of a Martensitic Transition in the Raman Spectra of Spontaneously Ordered GaInP Alloys. *Semicond. Sci. Technol.* **1998**, *13*, 1140.
63. Erol, A. *Dilute III-V Nitride Semiconductors and Material Systems: Physics and Technology*; Springer: Berlin, 2008; Vol. 105.
64. Fu, L.; Chtchekine, D.; Gilliland, G.; Lee, H.; Hjalmarson, H.; Yu, J.; Craford, M.; Wolford, D. J. Photoluminescence of Quasi-Direct Transitions in Disordered in In1-xGaxP Graded Gap Alloys. *IEEE J. Quantum Electron.* **1997**, *33*, 1123–1131.
65. Holtz, M.; Sauncy, T.; Dallas, T.; Seon, M.; Palsule, C.; Gangopadhyay, S.; Massie, S. Cryogenic Pressure and Lifetime Studies of a Defect Related Emission in Heavily Silicon Doped GaAs. *Phys. Status Solidi B* **1996**, *198*, 199–203.
66. Egerton, R. F. *Electron Energy-Loss Spectroscopy in the Electron Microscope*; Springer: Berlin, 1996; Vol. 233.
67. Rafferty, B.; Brown, L. Direct and Indirect Transitions in the Region of the Band Gap Using Electron-Energy-Loss Spectroscopy. *Phys. Rev. B: Condens. Matter Mater. Phys.* **1998**, *58*, 10326.
68. Onton, A.; Chicotka, R. Conduction Bands in In1−xAlxP. *J. Appl. Phys.* **1970**, *41*, 4205–4207.
69. Shah, J.; Miller, B.; DiGiovanni, A. Photoluminescence of AlxGa1−xAs. *J. Appl. Phys.* **1972**, *43*, 3436–3441.
70. Rockett, A. *The Materials Science of Semiconductors*; Springer: Berlin, 2007.
71. Vurgaftman, I.; Meyer, J.; Ram-Mohan, L. Band Parameters for III−V Compound Semiconductors and Their Alloys. *J. Appl. Phys.* **2001**, *89*, 5815–5875.